Received: 30 May 2018 | Revised: 2 April 2019 | Accepted: 13 April 2019
DOI: 10.1002/we.2355

WILEY

RESEARCH ARTICLE

On wind turbine loads during the evening transition period

Nan-You Lu[1] | **Sukanta Basu**[2] | **Lance Manuel**[1]

[1]Department of Civil, Architectural and Environmental Engineering, The University of Texas at Austin, Austin, Texas, USA
[2]Faculty of Civil Engineering and Geosciences, Delft University of Technology, Delft, The Netherlands

Correspondence
Lance Manuel, Department of Civil, Architectural and Environmental Engineering, The University of Texas at Austin, Austin, Texas, USA.
Email: lmanuel@mail.utexas.edu

Funding information
National Science Foundation (NSF), Grant/Award Number: CBET-1336304 and CBET-1336760

Abstract

The late afternoon hours in the diurnal cycle precede the development of the nocturnal stable boundary layer. This "evening transition" (ET) period is often when energy demand peaks. This period also corresponds to the time of day that is a precursor to late-afternoon downbursts, a subject of separate interest. To capture physical characteristics of wind fields in the atmospheric boundary layer (ABL) during this ET period, particularly the interplay of shear and turbulence, stochastic simulation approaches, although more tractable, are not suitable. Large-eddy simulation (LES), on the other hand, may be used to generate high-resolution ABL turbulent flow fields. We present a suite of idealized LES four-dimensional flow fields that define a database representing different combinations of large-scale atmospheric conditions (characterized by associated geostrophic winds) and surface boundary conditions (characterized by surface heat fluxes). Our objective is to evaluate the performance of wind turbines during the ET period. Accordingly, we conduct a statistical analysis of turbine-scale wind field variables. We then employ the database of these LES-based inflow wind fields in aeroelastic simulations of a 5-MW wind turbine. We discuss how turbine loads change as the ET period evolves. We also discuss maximum and fatigue loads on the rotor and tower resulting from different ABL conditions. Results of this study suggest that, during the ET period, the prevailing geostrophic wind speed affects the mean and variance of longitudinal winds greatly and thus has significant influence on all loads except the yaw moment which is less sensitive to uniform and symmetric incoming flow. On the other hand, surface heat flux levels affect vertical turbulence and wind shear more and, as a result, only affect maximum blade flapwise bending and tower fore-aft bending loads.

KEYWORDS

atmospheric boundary layer, evening transition, inflow, large-eddy simulation, turbulence, wind turbine loads

1 | INTRODUCTION

In recent years, wind energy has emerged as one of the fastest growing renewables; with this growth, some challenges for further development have become evident. Contemporary design standards—from, for example, the International Electrotechnical Commission (IEC)[1]—for turbine inflow generation do not cover the realistic dynamics and physics in the atmospheric boundary layer (ABL). Moreover, failures of turbines in service have drawn the attention of engineers especially due to the fatigue-sensitive composite materials used for blades. Such challenges served as motivation for us to propose generating a suite of physically realizable LES-ABL simulations and associated turbine loads evaluations that take into consideration inflow wind field spatial structure and characteristics that reflect a wide range of atmospheric conditions.

The evening transition, defined as a change over time in atmospheric stability from a convective boundary layer (CBL) to a neutral boundary layer (NBL), has a direct influence on the structure of the nocturnal boundary layer and the strength of low-level jets (LLJs). This transitional boundary layer has been a topic of interest of meteorologists for many years[2-5]; it has been found that large-scale forcings (eg, geostrophic winds[2]) as well as surface boundary conditions (eg, surface heat fluxes[3]) play important roles in the evolution of these transitional wind fields.

Additionally, power production would be impacted in these periods of enhanced electricity demands common during the evening transition.[6] As such, there is interest in an investigation of the characteristics of these transitional wind fields and of associated wind turbine loads.

Large-eddy simulation (LES), because of its relatively low computational cost for ABL simulations, has been successfully applied in the study of transitional wind fields in previous studies.[7-12] It is widely accepted that LES can describe physical details of atmospheric turbulence more realistically than conventional stochastic simulation approaches (such as TurbSim[13]) and can thus be expected to also simulate evening transition wind fields more accurately. Moreover, LES can also be combined with mesoscale models (eg, the Weather Research and Forecasting Model, WRF) to improve dynamical and physical representations in ABL simulations.[11]

To generate inflow fields for assessment of wind turbine loads using LES, previous studies have shown that conventional stochastic simulation is deficient in representing physical details of wind fields in the stable boundary layer (SBL); this, in turn, affects the accuracy of associated turbine loads.[14,15] Park et al[16] developed a framework for carrying out LES-ABL simulations and performed a statistical analysis of both wind field characteristics and turbine loads in the SBL. This framework allows similar studies of other LES-generated inflow wind fields and associated turbine loads, such as during the ET period. In the present study, we extend the earlier simulation study and framework[16] to investigate these ABL transitional condition wind fields and wind turbine loads that result then.

In the following paragraphs of Section 2, we introduce some background on the LES model, the framework for the LES-ABL computations, and the procedure for inflow field generation for eventual assessment of wind turbine loads. Next, in Section 3, we summarize the statistical analyses of the simulated ET wind fields with an emphasis on the relationships among turbine-scale wind field variables and the influence of full-domain "external" variables on them. Turbine load statistics are discussed in Section 4 with an explanation of how the external variables (interacting with the turbine blade pitch control system) influence both fatigue and maximum turbine loads. Spectral analyses of the turbine loads are also conducted and support the results of the previous statistical analyses. Finally, we present the most significant findings and conclusions from this study and discuss how this work lays the foundation for other planned research including studies involving the simulation of downbursts which are common in the late-afternoon period during or after the ET period. Note that control systems are of special interest during transient events such as downburst; hence, in the simulated ET fields that precede downburst, we consider the importance of pitch control to allow comparison of this same control during downbursts.

2 | METHODOLOGY

2.1 | Background of LES

To study flow fields in the ABL, large-eddy simulation is the preferred method of choice due to its computational efficiency in computations for such high Reynolds number turbulent flows.[17] To achieve the needed efficiency, this approach works with filtered Navier-Stokes equations:

$$\frac{\partial \tilde{u}_i}{\partial t} + \frac{\partial \left(\tilde{u}_i \tilde{u}_j\right)}{\partial x_j} = -\frac{1}{\rho}\frac{\partial \tilde{p}}{\partial x_i} + \delta_{i3} g \frac{\tilde{\theta} - \langle \tilde{\theta} \rangle}{\theta_o} + f_c \varepsilon_{ij3} \tilde{u}_j + \nu \frac{\partial^2 \tilde{u}_i}{\partial x_j \partial x_j} + \tilde{F}_i - \frac{\partial \tau_{ij}}{\partial x_j}, \tag{1}$$

where t represents time; u_j, the velocity component in direction, j; x_j, the spatial coordinate in direction, j; θ, the potential temperature; θ_o, the reference potential temperature; p, the dynamic pressure; ρ, the density of air; ν, the kinematic viscosity; δ_{i3}, the Kronecker delta function; ε_{ij3}, the alternating unit tensor; g, the gravitational acceleration; f_c the Coriolis parameter; F_i, the forcing term; and τ_{ij}, the subgrid-scale (SGS) stress term. One can neglect the molecular diffusion term owing to the extremely high Reynolds number and the nonresolved viscous processes in the atmosphere near the ground. The delimiters, $\langle\rangle$, indicate averages of the corresponding variable over a horizontal plane. The tilde modifier denotes operation with a spatial filter of characteristic width, Δ_f, which is generally on the order of a few meters for ABL simulations; for turbulence features at a scale smaller than Δ_f, a subgrid-scale model is introduced. For ABL simulations, an eddy-viscosity model, such as the Smagorinsky model, is widely used to model the stress term, τ_{ij}; this is done here as well. Another filtered equation for potential temperature is also solved together with the filtered Navier-Stokes equation for nonneutral ABL simulations.

The large-eddy simulation for generating ABL turbulent flow fields is carried out using an in-house code.[18,19] Derivatives in the horizontal directions and in the vertical direction are approximated using a Fourier collocation method and a second-order central difference scheme, respectively. An explicit second-order Adams-Bashforth time advancement scheme is employed. Coriolis terms are considered only for horizontal winds, and forcing terms are imposed by the geostrophic wind. A tuning-free SGS model, which is referred to as the LASDD (locally averaged scale-dependent dynamic) model, is utilized in all the turbulence simulations.

2.2 | LES-ABL computations

Large-eddy simulation is employed to generate wind velocity fields in the atmospheric boundary layer during the evening transition period. We select different combinations of full-domain environmental conditions and boundary conditions as input parameters in order to generate the wind fields for the convective boundary layer (CBL). To generate the ET wind fields, the following initialization settings are used:

$$\begin{aligned} U(z) &= G && \text{for} \quad z > z_o \\ V(z) &= 0 && \text{for} \quad z > z_o \\ W(z) &= 0 && \text{for} \quad z > z_o \\ \Theta(z) &= 300 && \text{for} \quad z_o < z \leq H_i \\ \Theta(z) &= 300 + N(z - H_i) && \text{for} \quad z > H_i, \end{aligned} \tag{2}$$

where $U(z)$, $V(z)$, and $W(z)$ are the mean velocity (m/s) components in the longitudinal, lateral, and vertical directions, respectively, at height z(m) above ground; G is the geostrophic wind speed (m/s); $\Theta(z)$ is the mean potential temperature (K); z_0 is the aerodynamic roughness length (m); H_i is the initial boundary layer height (m); and N is the inversion strength (K/m). To generate turbulence, Gaussian perturbations with standard deviations of 0.1 m/s and 0.1 K are added to the initial vertical velocity and potential temperature fields, respectively. The initialized fields are evolved in time by solving the filtered Navier-Stokes equations, subject to the constraints defined by the large-scale forcing terms and boundary conditions, to generate a 2-hour LES-based wind velocity field. The first hour of spin-up is discarded in order to guarantee a well-developed inertial range in the resulting spectra of the simulated flow fields.

Among all the LES inputs, we focus on two external variables—the geostrophic wind speed G (m/s) and the surface sensible heat flux (henceforth, surface heat flux) H_s (K-m/s)—as we investigate characteristics of the ET wind fields and associated turbine loads. Table 1 shows 12 combinations of different G and H_s values used for the various LES settings in this study. Run No. 4 (denoted as "control" in the table) is selected as a baseline for comparison against other cases in subsequent discussion. The geostrophic wind speed, G, is a constant forcing value for each LES run, while the surface heat flux, H_s, serves to establish a lower boundary condition for the CBL and has a constant value for the first hour and decays to zero using a cosine function over the second hour. The evolution of the overall stability of the convective boundary layer due to this decaying condition is shown in Appendix A. Other external variables are also required for the LES model but these are held constant (eg, the aerodynamic roughness length z_0 is set as 0.1 m; the initial boundary layer height H_i is 500 m; the inversion strength N is 0.003 K/m; and the Coriolis frequency f is 10^{-4} s^{-1}), thus ruling out their effects in this study.

In the LES computations, the domain size is set at 10 000 m × 10 000 m × 2000 m and uses a 360 × 360 × 72 grid. Monin-Obukhov similarity theory is applied at the lower boundary, while a zero-stress condition is employed at the upper boundary. The lateral boundary conditions are assumed periodic. The first grids above ground level are located at a height of 13.89 m, which is half the grid spacing in the vertical direction. A time step of 0.25 second is selected; thus, there are a total of 28 800 time steps for each 2-hour run. In order to generate inflow fields for the wind turbine model, a 2D spatio-temporal field with dimensions 360m(y) × 72m(z) × 240seconds(t) is extracted from the middle cross-section (y-z plane) of the full 3D domain output. These 2D data serve as the inflow input for the aeroelastic simulation that are used to yield turbine loads. Figure 1 provides details about the computational domain used in the simulations. Table 2 provides a summary of relevant information for the LES computational framework.

2.3 | Turbine-scale inflow generation

Figure 2 schematically presents the framework for the LES-ABL computations and describes details related to turbine-scale inflow generation for loads assessment. After obtaining the 2D LES-based wind velocity fields, we extract five nonoverlapping flow-field slices from the bottom of

TABLE 1 List of LES runs with different combinations of external variables

Run No.	1	2	3	4 (CONTROL)	5	6	7	8	9	10	11	12
G, m/s	10	10	10	12	12	12	15	15	15	18	18	18
H_s, K-m/s	0.00	0.01	0.05	0.00	0.01	0.05	0.00	0.01	0.05	0.00	0.01	0.05

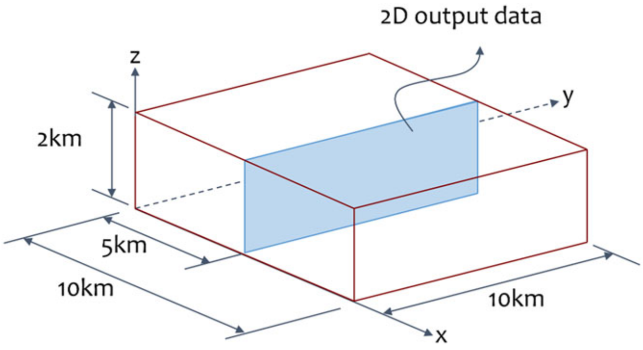

FIGURE 1 Computational domain for the large-eddy simulation [Colour figure can be viewed at wileyonlinelibrary.com]

TABLE 2 Relevant information for the LES computational framework

Domain	10 km × 10 km × 2 km
Grid points	360 × 360 × 72
Time step	0.25 s
No. of time steps	28 800
Simulation time	2 h
Spin-up time	1 h

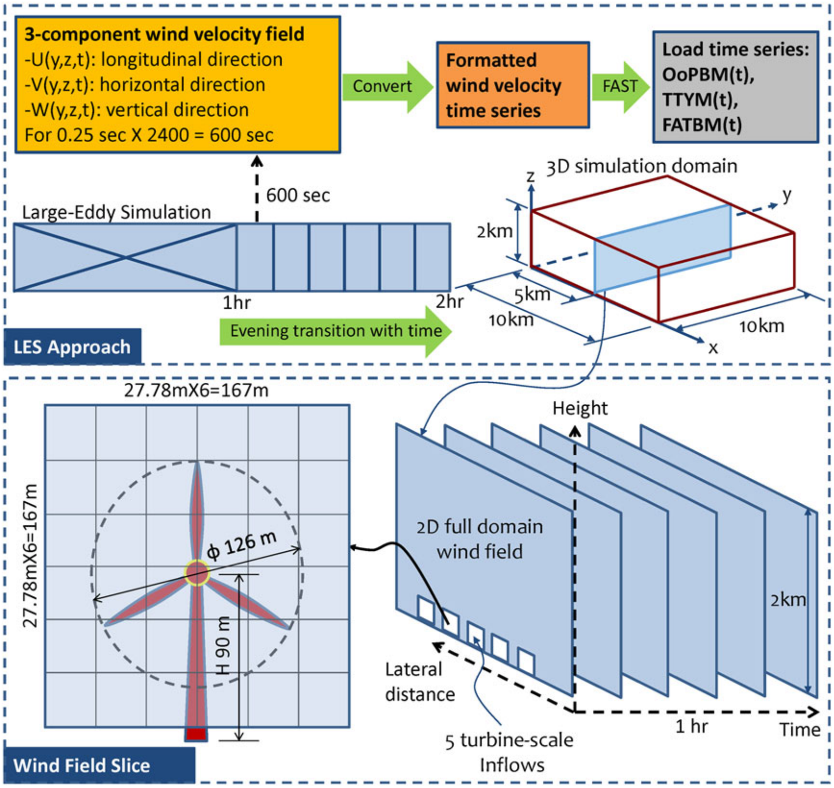

FIGURE 2 Temporal (top) and spatial (bottom) segmentations of the LES wind velocity fields [Colour figure can be viewed at wileyonlinelibrary.com]

the 2D domain along the lateral direction. These slices are selected so as to cover a vertical distance ranging from z = 14 m to z = 181 m as the tips of the blades of the selected 5-MW turbine model span a vertical distance ranging from 27 to 153 m above ground level. Adjacent 2D field lateral slices are separated by a distance equal to at least five times the rotor radius so as to limit correlation in the wind field characteristics of the individual slices. As stated, the first hour during spin-up in the LES computation is discarded; the time series representing the second hour are separated into six 10-minute segments that serve as distinct flow fields for subsequent analyses. As such, 30 sets of flow fields are generated for each of the 12 LES cases (Table 1), yielding a total of 360 flow fields that form the ET database for wind field statistical analysis and serve as inflow for the turbine loads assessment.

2.4 | Turbine model for load simulations

In this study, the NREL 5-MW Onshore Baseline Wind Turbine model[20] is used to carry out all the turbine response simulations. The model captures the characteristics of a conventional three-bladed upwind turbine with a variable-speed and collective pitch-control system. Selected properties and dimensions of the turbine model are presented in Table 3. The open-source program, FAST V8,[21,22] for aeroelastic simulation, is utilized to obtain turbine load time series resulting from the selected inflow fields. These time series of simulated loads on various components of the turbine are used in the analysis of both fatigue and maxima. A blade pitch control system is activated in the model when the inflow wind speed is greater than the rated wind speed of 11.4 m/s; a rotor rotation speed of 12.1 rpm is maintained when the turbine is pitch-controlled. Natural frequencies of the NREL 5-MW baseline turbine can be determined via periodic linearization analysis[23] in FAST. For the onshore configuration, the natural frequencies of the first tower fore-aft bending mode and the first blade flap bending mode are found to be 0.3240 and 0.6993 Hz, respectively.[20] The different LES runs resulted in wind velocity fields at ~ 28 m resolution; we acknowledge that this spatial resolution is at the limit

TABLE 3 Selected wind turbine model properties and dimensions

Properties and Dimensions	Values
Power rating	5 MW
Rotor orientation	Upwind
Rotor configuration	3 blades
Rotor diameter	126 m
Hub height	90 m
Cut-in, rated and cut-out wind speeds	3, 11.4, and 25 m/s
Cut-in and rated rotor speeds	6.9 and 12.1 rpm
Rotor mass	110 000 kg
Nacelle mass	240 000 kg
Tower mass	347 460 kg

for achieving acceptably accurate loads for the 5-MW turbine (see, for example, Rai et al[24] and Sim et al[14]). Nevertheless, the important energetic structural modes of vibration, evident in power spectra for all the turbine loads studied, are accounted for. Besides, the study by Rai et al[24] used a finite-volume-based solver with intrinsic numerical dissipation issues (see Glendening and Haack[25] for related discussions); in such approaches, the effective resolution can be four to seven times greater than the computational grid size. Moreover, they used a static SGS which can lead to additional dissipation. In Sim et al[14] and in the present study, we use a pseudo-spectral code, with significantly less numerical dissipation issues and we also adopt a dynamic SGS scheme. When one takes these differences into consideration, spatial resolution utilized by us and the previous studies are quite similar; additionally, we note that there are significant challenges associated with LES computations of finer resolution (than ~28 m resolution) and a large computation domain when using a pseudo-spectral code with a dynamic SGS model. For these reasons and because Sim et al[14] showed that spatial resolution did not have a great impact on loads, we employed the computational scheme described in this study.

2.5 | Fatigue and maximum loads

We are interested in both maximum and fatigue loads during the ET period and accordingly undertake a statistical analysis of these loads using all the 360 FAST simulations. The maximum load (MAX) refers to the largest value of the selected load measure that occurs in a 10-minute time series; additionally, a 1000-cycle "equivalent fatigue load" (EFL), alternatively referred to as a 0.6-second or 1.67-Hz damage-equivalent load, is used when considering fatigue. This EFL measure is defined as follows[26]:

$$EFL = \sqrt[m]{\sum_{i=1}^{N} \frac{S_i^m}{1000}}. \tag{3}$$

According to this definition, the accumulated damage due to 1000 stress cycles of constant amplitude equal to EFL is the same damage as that due to the actual N cycles of variable amplitude, S_i, that result in each simulated 10-minute time series (also, m is the Wöhler exponent taken to be 10 for carbon-fiber composite blades, 6 for high-quality steel as with nacelle components, and 3 for the steel tower). This convenient definition of EFL for fatigue loads is such that a 10-minute load time series that places more fatigue demand on a turbine component due to simulated S_i levels will lead to higher EFL values; note that the choice of 1000 cycles is arbitrary and does not affect conclusions drawn. The particular choice of 1000 refers to stress amplitude cycles with an average rate of five cycles every 3 seconds (1.67 Hz).

3 | CHARACTERISTICS OF LES-BASED WIND FIELDS

3.1 | Mean wind profiles during the evening transition period

The LES-based wind fields during the evening transition period start from a convective boundary layer and end up in a neutral boundary layer. It is interesting to study the mean wind speed profiles as these can greatly influence wind turbine loads. Wind speed values at all the lateral computational grid points are averaged to derive a mean profile that describes the entire wind field. We should note that, in this study, we take planar averages from instantaneous wind fields generated by the LES model instead of temporal averages. Such profiles are plotted at different times separated by 10 minutes (ie, at 10, 20, …, 60 minutes). In this way, characteristics of these mean wind fields can be captured more easily on plots that then describe the evolution of the wind profile clearly. Here, we do not focus on the near-wall characteristics of velocity profiles but provide additional velocity profile information in Appendix B. Figure 3 shows such averaged wind profiles varying with time for a geostrophic wind speed equal to 12 m/s. Two cases with surface heat flux equal to 0.00 and 0.05 K-m/s are plotted for comparison. Two different spatial scales that cover the entire simulation vertical domain (left) and the turbine vertical scale (right) are depicted. As expected, the wind speed matches the geostrophic wind speed at regions above the influence of the boundary layer. An increasing geostrophic wind speed, as

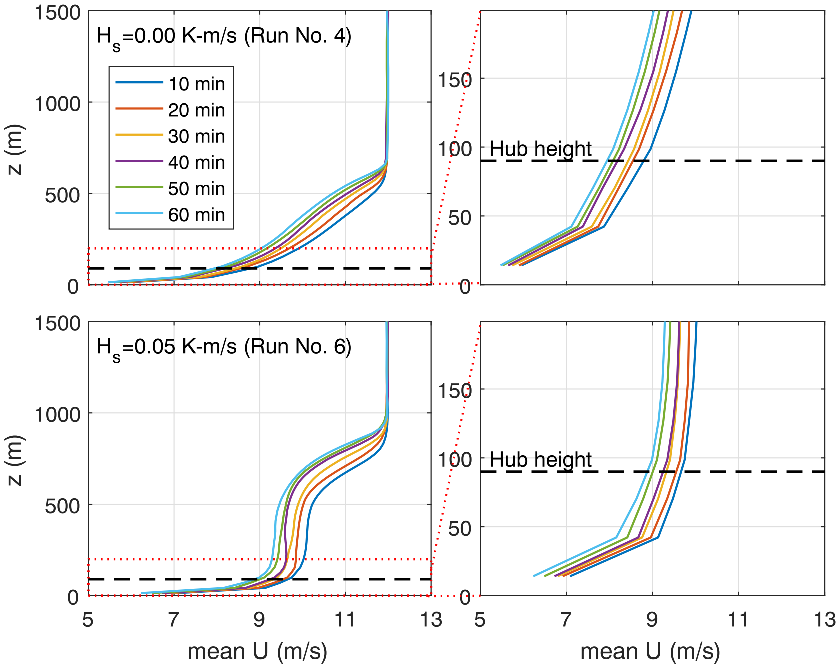

FIGURE 3 Evolution of longitudinal wind profiles for an evening transition boundary layer ($G = 12$ m/s). The cases with surface heat flux 0.00 and 0.05 K-m/s are selected (ie, Run Nos. 4 and 6 in Table 1). Left: ABL; right: zoomed-in portion over the turbine scale [Colour figure can be viewed at wileyonlinelibrary.com]

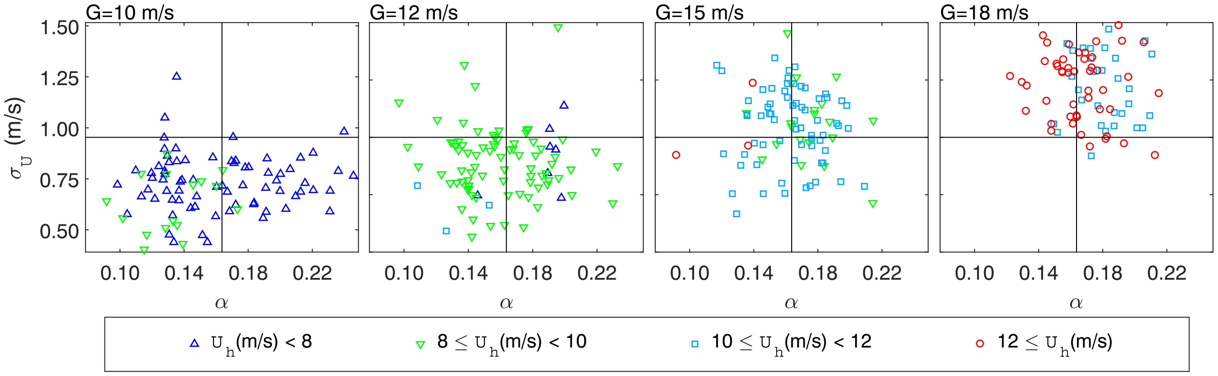

FIGURE 4 Relationships between wind shear, α, and turbulence standard deviation, σ_U, classified by longitudinal wind velocity, U_h, based on 360 LES-generated wind fields for the four different geostrophic wind speeds. The data are centered at the mean values of α and σ_U [Colour figure can be viewed at wileyonlinelibrary.com]

expected, leads to larger longitudinal wind speeds at hub height. On the other hand, increasing the heat flux distorts the shapes of the profiles and decreases estimated exponents of a power-law fit to surface winds. In other words, with an increase in heat flux, the wind speed increases over the scale of the turbine but decreases around 200 to 500 m above ground level (AGL); together, these effects lead to reduced wind shear. In summary, an increase in surface heat flux leads to larger longitudinal wind speeds but smaller wind shears at the turbine hub height. In addition, turbine-scale wind profiles are seen to decay with time during the one hour with decreasing instability.

3.2 | Turbine-scale flow field variables

We compute turbine-scale flow field statistics from the 360 LES wind velocity time series to investigate characteristics of these ET winds. Several turbine-scale statistics during the ET period are considered—of greatest interest in wind turbine loads assessment are the mean wind velocity at hub height in the longitudinal direction, U_h, the standard deviation of the longitudinal wind velocity component at hub height, σ_U, and the estimated wind shear exponent, α, based on an assumed power law wind shear profile. We are also interested in inter-relationships among these parameters. In Figure 4, statistics extracted from the 360 flow fields are summarized so that all three of these turbine-scale wind field descriptors may be studied together. The data in Figure 4 are separated based on the values of U_h indicated by different colors and symbols. The four cases with different geostrophic wind speeds are best discussed by studying four quadrants for each case. For $G = 10$ m/s, it is clear that the data are largely distributed in the lower-left quadrant where U_h and σ_U values are both small. As the geostrophic wind speed increases, U_h and σ_U

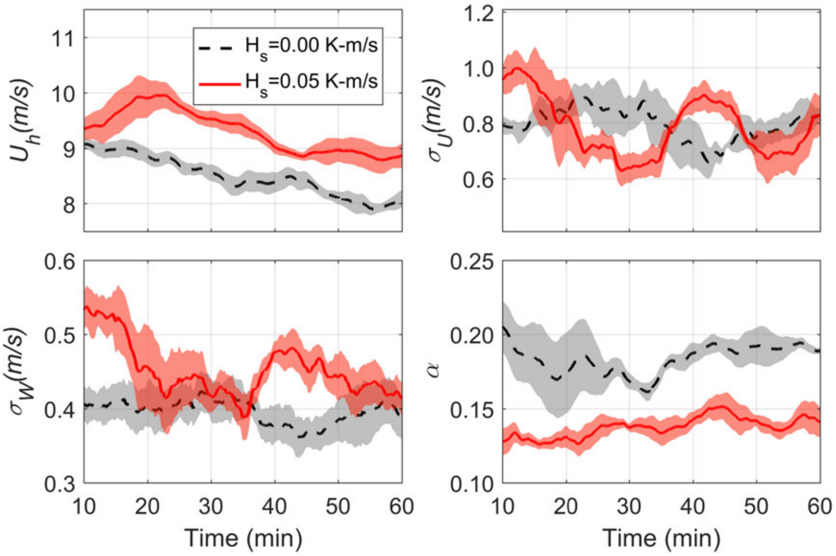

FIGURE 5 Variations of turbine-scale wind field variables with time for the cases of $G = 12$ m/s with different surface heat fluxes. Data are extracted from each 10-minute moving window; five samples are used to estimate the means (lines) and standard deviations (shaded regions) [Colour figure can be viewed at wileyonlinelibrary.com]

values also increase and most of the data move toward the upper-right quadrant. The results suggest that, for the ET flow fields, wind shear and turbulence are positively correlated with each other. However, this correlation appears to be weaker for lower longitudinal wind speeds since the variation in wind shear is seen to be greater. It is clear from the figure that there is also positive correlation between longitudinal wind speed and turbulence levels as evidenced by the data distribution that moves from the bottom to the top quadrants in the plots as the hub height wind speed, U_h, increases.

The characteristics of wind fields during the ET period can be seen by studying the variation in the turbine-scale flow field statistics with time. Figure 5 shows how the selected turbine-scale variables, U_h, σ_U, σ_W (standard deviation of vertical wind speed at hub height) and α, extracted every 10 minutes, change with time during the ET simulations. The ensemble mean values (center lines within the error bands) and standard deviations (error band widths) are computed from the wind data of the five extracted flow fields for each 10-minute duration throughout the 1 hour of simulation time. With the geostrophic wind speed fixed at 12 m/s, we select surface heat flux values as 0.00 and 0.05 K-m/s for comparison. The black dashed lines represent the control case. This neutral case (with $H_s = 0.00$ K-m/s) is expected to have less initial turbulence than the $H_s = 0.05$ K-m/s case whose stability changes from convective to neutral during the evening transition. As seen in the figure, the hub height longitudinal wind speeds (U_h) for both cases decay with time as is expected based on earlier discussions involving the evolution of mean wind profiles (Figure 3). Note that data from 360 locations are taken in Figure 3, while only data from the five slices are used in Figure 5. An unexpected peak appears at about 20 minutes in the nonneutral case probably due to localized turbulence, but the decreasing trend is evident for the overall 1 hour. However, the longitudinal turbulence (σ_U) does not change much during the ET period, whereas the vertical turbulence (σ_W) for the convective case has a clear decreasing trend. The results reveal that the stability change during the evening transition influences the vertical wind turbulence but has little effect on the longitudinal wind turbulence. The different components of wind field turbulence affect different turbine load types, as is discussed in the next section. From the variation in wind shear (α) during the ET period, a slightly increasing trend is evident in the convective case. The neutral case with no change in stability keeps the mean wind shear at about the same level during the ET period.

3.3 | Influence of external flow field variables on turbine-scale variables

We discuss the influence of full-domain “external” flow field variables—geostrophic wind speed and surface heat flux—on various turbine-scale wind field variables. Figure 6 shows cumulative distribution functions (CDFs) calculated from 10-minute time series of the longitudinal (left panels) and vertical (right panels) wind speed at hub height. For the CDFs in the top panels, the data for the neutral cases with zero surface heat flux are presented to compare the influence of geostrophic wind speed. It is clearly seen that the mean value of the longitudinal wind speed increases with an increase in geostrophic wind speed, whereas the vertical wind speed does not change much. In addition, the range of this longitudinal wind speed also gets larger as G increases, by examining, for instance, the spread in wind speed values for CDF equal to 0.10 and 0.90 (the horizontal dotted lines). The largest spread is seen for the $G = 18$ m/s case which, as we saw earlier in Figure 4, has the greatest turbulence levels. It is concluded then that larger geostrophic wind speeds lead to increases in the mean and variance of longitudinal wind speeds at hub height (ie, increases in U_h and σ_U). In the study of CDFs in the bottom panels, the geostrophic wind speed is held fixed at 12 m/s, and the surface heat fluxes are varied. Both the longitudinal and vertical mean wind speeds at hub height (ie, W_h) do not vary much with heat flux, but the variance of the vertical wind speed (ie, σ_W) increases slightly with greater H_s. It is well-known that the vertical velocity field will exhibit a skewed

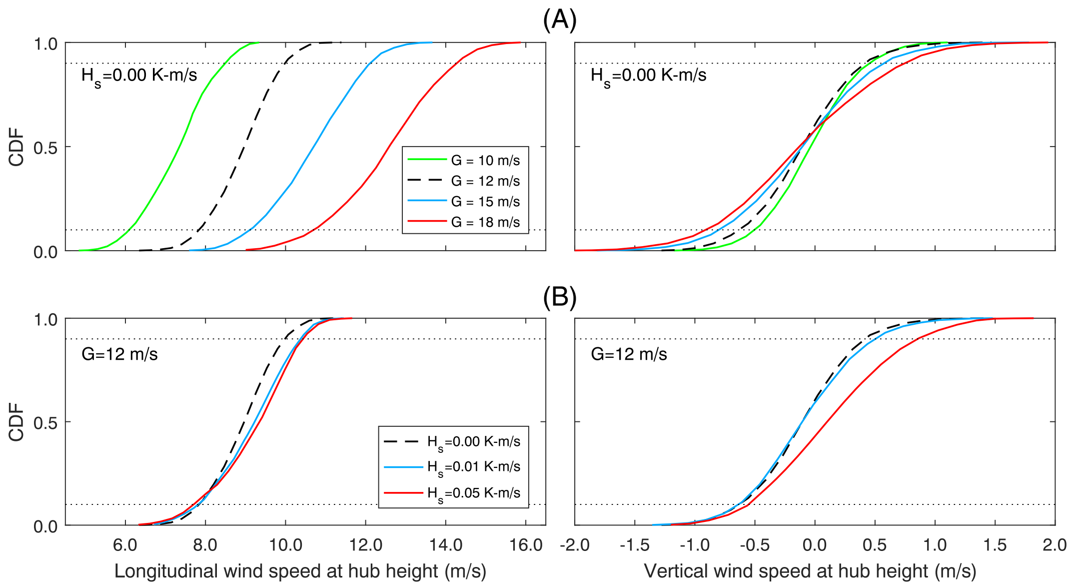

FIGURE 6 Cumulative distribution functions (CDFs) of A, hub height longitudinal and vertical wind speeds for cases with different geostrophic wind speeds ($H_s = 0.00$ K-m/s, top panels) and B, hub height longitudinal and vertical wind speeds for cases with different surface heat fluxes ($G = 12$ m/s, bottom panels). The first 10-minute time series of the five extracted flow fields are used. Dotted lines are drawn at 0.10 and 0.90 quantiles [Colour figure can be viewed at wileyonlinelibrary.com]

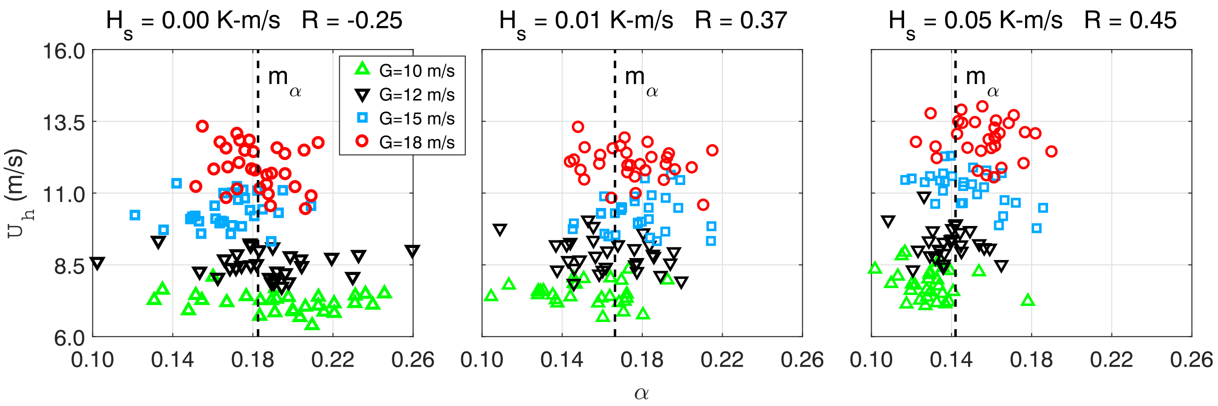

FIGURE 7 Variation of turbine-scale wind field statistics extracted from 10-minute time series with changes in surface heat flux, for different geostrophic wind speeds (R denotes the Pearson correlation coefficient between the wind shear exponent and hub height longitudinal mean wind speed) [Colour figure can be viewed at wileyonlinelibrary.com]

distribution. For a horizontal cross-section taken at a given height, one will generally only see a few strong updrafts with small areal coverage that are surrounded by weak downdrafts with large spatial coverage. An example of visualization of the cross-sectioned flow field for a neutral case is provided in Appendix C, which also shows the evident coherent structures. On average, the mean is zero but we expect to see strong updrafts as we do in the CDF for W_h. The CDF in the higher surface heat flux case is found to have longer upper tails explained by an increase in the extreme vertical wind speeds in the upward direction. In summary, surface heat flux levels that drive the mixing of air at the surface can enhance the turbulence intensity especially in the vertical winds.

Figure 7 shows scatter plots of wind field statistics (wind shear and hub height longitudinal wind speed) for three different surface heat flux values; the data are separated out according to geostrophic wind speed. In the plots, R indicates the sample Pearson correlation coefficient between the two variables, α and U_h. The vertical dashed lines represent the mean values of wind shear in each case. First, it is quite clear that higher geostrophic wind speeds leads to larger hub height longitudinal wind speeds as expected. Second, the data suggest that larger heat flux levels result in stronger positive correlation between U_h and α. The variability in wind shear at lower wind speeds is especially large in the neutral case. Note that the larger heat flux cases (eg, $H_s = 0.05$ K-m/s) are accompanied by relatively lower wind shear levels, which result from greater mixing (ie, turbulence).

In summary, we see that the geostrophic wind speed influences the mean and variance of longitudinal wind speeds at hub height to a great extent, while the surface heat flux variation affects vertical turbulence and wind shear more. Turbine-scale wind field variables can influence different types of turbine loads resulting from the associated inflow fields; this is discussed in the next section.

4 | TURBINE LOADS ASSESSMENT

In the statistical analysis of wind turbine loads, we focus on the following load variables: the blade root out-of-plane bending moment (OoPBM), the fore-aft tower base moment (FATBM), and the tower-top yaw moment (TTYM), as defined in Figure 8. These three turbine loads have contrasting characteristics and are often of interest when studying turbine performance under various external conditions such as during the evening transition period. We are interested in maximum loads as well as fatigue loads, as defined in Section 2.5.

4.1 | Turbine load time series and blade pitch control effects

The characteristics of the load time series are first studied in order to assess the variation in wind inflow and loads with time. The effect of the turbine blade pitch control system can also be assessed by studying the variation in the blade pitch angle change and the resulting loads. The ET period is right around the time thunderstorm downbursts are most likely to occur. The important role of pitch control during those transient events has been well-documented in earlier studies[27,28]; because the ET period is a precursor to such events, it is useful to assess pitch control effectiveness during this ET period first. Figure 9 shows a 10-minute segment time series for the hub height longitudinal mean wind speed, U_h, the blade pitch angle, and the three selected loads. Only cases with zero surface heat flux are considered so that the cases with geostrophic wind speed equal to 15 and 18 m/s can be compared. Since pitch control actions are only triggered when the hub height wind speed exceeds the rated wind speed (11.4 m/s), the two cases with G = 10 and 12 m/s are not included as activation of the pitch control does not occur much in the simulated time series. For the case with G = 15 m/s, pitch control is activated for only a short period of time (~50-100 s). During that period, load levels for the case with pitch control are slightly lower than when no pitch control is assumed. The differences are clearer in the G = 18 case where, for a larger number of time segments, the hub height wind speed exceeds the rated wind speed. The OoPBM and FATBM loads are found to be more sensitive to pitch control than TTYM; pitch control most directly influences loads affected by wind forces normal to the rotor plane.

The pitch control effects can be further evaluated by examining statistical data from the 360 10-minute simulations as done in Figure 10. The scatter plots show the relation between longitudinal mean wind speed at hub height and maximum OoPBM, FATBM, and TTYM loads. All the statistics are normalized so as to have a zero mean and unit standard deviation (ie, normalization is with respect to the ensemble mean from the 360 simulations). The data points with and without pitch control are plotted in blue and red, respectively. It is clear that pitch control action considerably decreases OoPBM and FATBM maximum loads for higher hub height wind speeds; for the TTYM loads, this pitch control influence is reduced. The results also reveal that the pitch control system has no influence on maximum loads for the cases of G = 10 and 12 m/s (the triangle markers). The maximum load levels for OoPBM and FATBM are almost the same at the higher longitudinal wind speeds (square and circle markers) because the effects of the aerodynamic forces due to the inflow winds are suppressed by pitch angle changes of the turbine blades.

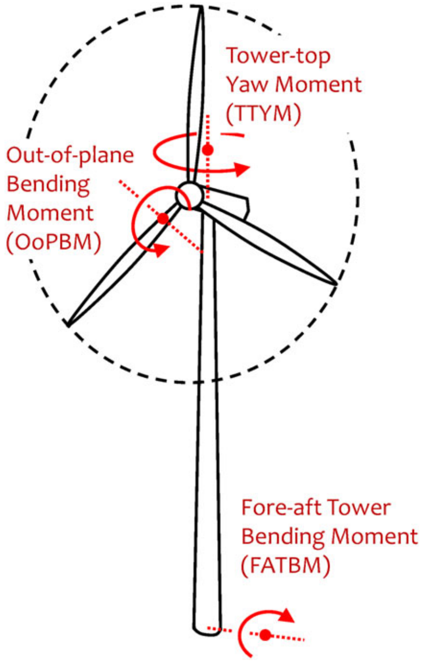

FIGURE 8 Schematic diagram showing the three types of turbine loads, OoPBM, FATBM, and TTYM, used in this study [Colour figure can be viewed at wileyonlinelibrary.com]

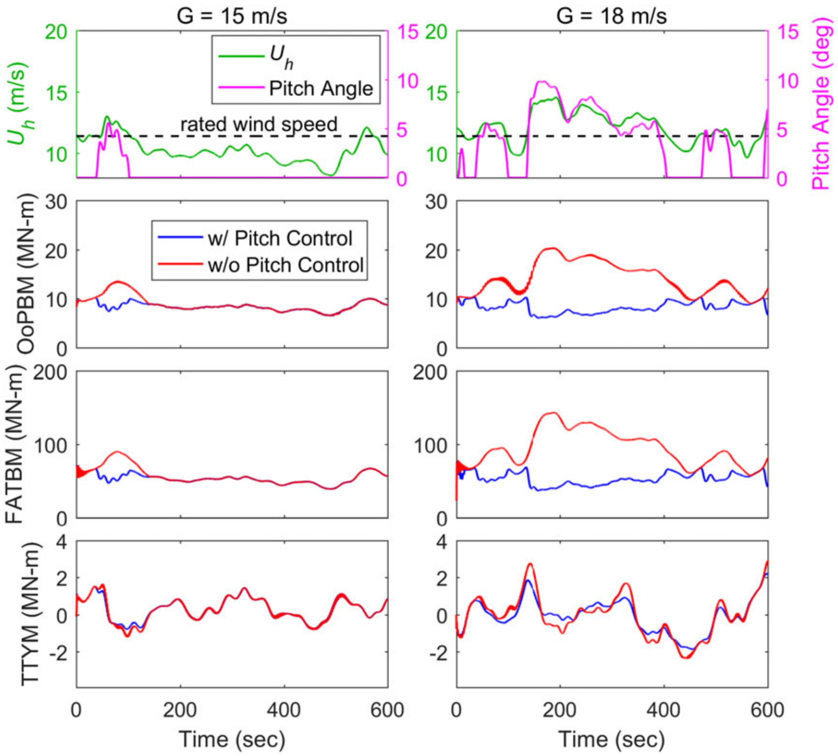

FIGURE 9 Selected 10-minute time series of hub height longitudinal wind speed, pitch angle, OoPBM, FATBM, and TTYM. Comparisons are for the neutral case (H_s = 0.00 K-m/s) with geostrophic wind speed equal to 15 m/s (left panels) and 18 m/s (right panels). The load time series are presented for cases, both with and without pitch control [Colour figure can be viewed at wileyonlinelibrary.com]

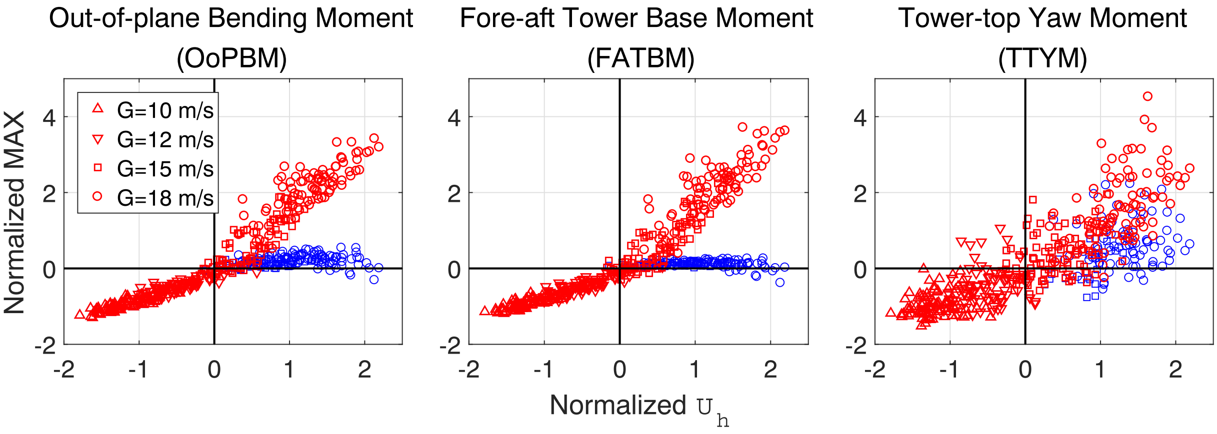

FIGURE 10 Scatter plots of normalized data for hub height longitudinal mean wind speed U_h versus maximum loads of three types for four different geostrophic wind speeds. Data points with pitch control (blue) and without pitch control (red) are shown. All data are normalized to have zero mean and unit standard deviation [Colour figure can be viewed at wileyonlinelibrary.com]

4.2 | Influence of turbine-scale inflow field variables on turbine loads

We consider a simple linear regression model to relate maximum and fatigue load statistics to various turbine-scale inflow parameters, x_i, as follows:

$$\text{Turbine Load Statistic (EFL or MAX)} = C_0 + \sum_i C_i x_i, \tag{4}$$

where C_0 and C_i are estimated using the loads data from the 360 10-minute simulations; x_i serve as "predictor" variables. All the variables are normalized to have zero mean and unit standard deviation. A total of six turbine load statistics (representing fatigue and maximum loads, ie, EFL and MAX for OoPBM, FATBM, and TTYM) are studied.

Figure 11 shows the estimated coefficients, C_i, for seven different turbine-scale inflow parameters. In the model based on Equation (4), only inflow parameters whose P values are less than .05 are included. If the P value for corresponding to any x_i is greater than .05 for any load statistic, that parameter is not included in the model for that load statistic and C_i is set to zero. In regression, the P value for each predictor variable tests the null hypothesis that the corresponding coefficient is equal to zero (ie, has no effect). A low P value (below .05) indicates that the null

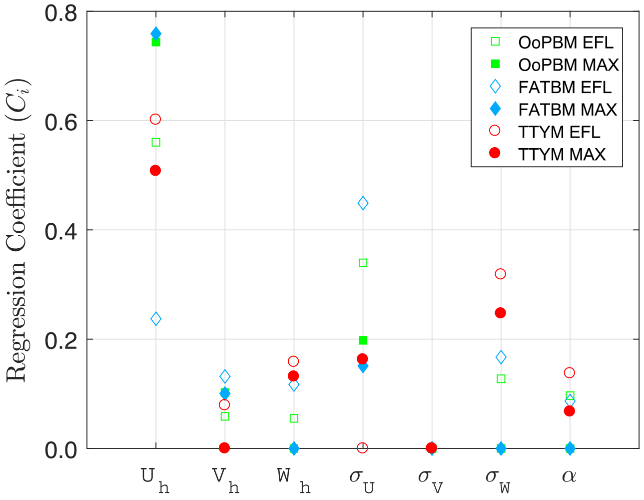

FIGURE 11 Model coefficients for turbine fatigue loads (EFL) and maximum loads (MAX) resulting from regression on normalized turbine-scale inflow parameters [Colour figure can be viewed at wileyonlinelibrary.com]

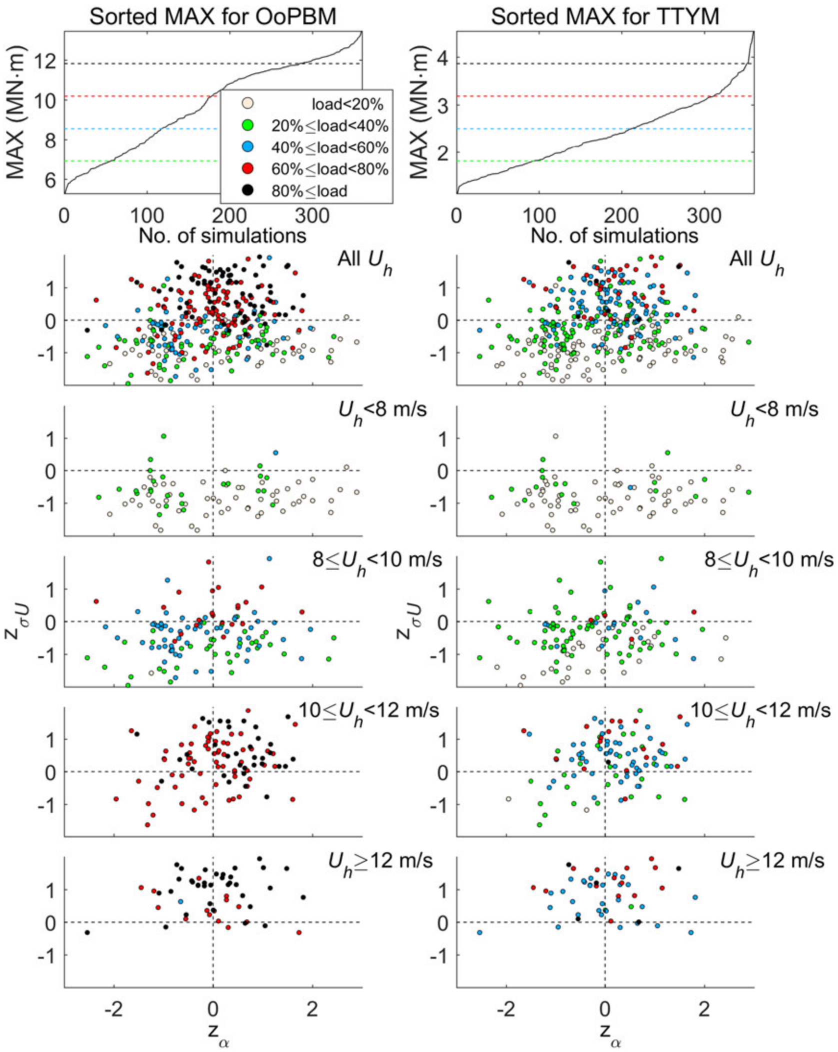

FIGURE 12 Maximum load statistics of OoPBM and TTYM (in MN-m) versus turbine-scale inflow field parameters. Note that z_α and $z_{\sigma U}$ denote normalized values of wind shear and standard deviation of hub height longitudinal wind velocity, where normalization results in a zero mean and unit standard deviation. The top two panels show the sorted nonnormalized maximum loads versus the number of utilized simulations. The entire load range in each case is equally separated into five levels [Colour figure can be viewed at wileyonlinelibrary.com]

hypothesis may be rejected—ie, a predictor with a low *p* value is a meaningful addition to the regression model since changes to that predictor's value leads to changes in the response variable (predictand).

From Figure 11, we see that turbine-scale inflow parameters influencing turbine loads the most are U_h, σ_U, σ_W, and α. In particular, the hub height longitudinal mean wind velocity, U_h, has predominant influence on all load statistics and especially so on maximum loads. An exception is maximum TTYM loads where the vertical wind velocity component's standard deviation has a large contribution (the vertical mean wind is also important). For FATBM fatigue loads, we note that there is greater influence of σ_U than of U_h; turbulence associated with longitudinal winds influences fatigue loads more than the mean component does. For TTYM loads, the vertical wind turbulence, σ_W, has larger influence than longitudinal turbulence. Wind shear (through the parameter, α) influences all the fatigue loads and the TTYM maximum loads. In summary, OoPBM and FATBM loads are influenced most by the longitudinal wind; U_h has dominant contribution but the influence of σ_U is noted especially for in fatigue loads. TTYM loads are associated with rotation in a horizontal plane that is associated with nacelle yaw; U_h still has dominant influence but σ_W and α have secondary contributions that are comparable with or greater than that of the longitudinal turbulence, σ_U. TTYM fatigue loads, for instance, are related to the variance of the load time series which is noticeably influenced by σ_W and α; all fatigue load statistics, in general, show significant contributions from these two parameters.

Results derived from analyses of the turbine loads may be further examined by studying scatter plots of the load statistics and their variation with different turbine-scale inflow field parameters. Figure 12 shows OoPBM and TTYM maximum load statistics (MAX in MN-m) for different U_h, σ_U, and α values. (For the sake of brevity and to highlight contrasts among the three load types, FATBM MAX statistics are not included.) The sorted data at the very top serve to indicate the distribution of the loads resulting from the 360 simulations. For instance, for OoPBM, a significant portion of the sample had maxima that were in the 60 to 80 percentile group; likewise, for TTYM, it is clear that only a very small sample of maxima accounted for the highest 20% of the maxima. The color scale used for the load statistics is an indication of magnitude; load statistics from all the 360 simulations are separated by groups based on the hub height longitudinal wind speed, U_h. Generally, the data suggest that maximum loads increase for larger U_h values as well as for larger σ_U values. The influence of wind shear on turbine load maxima is comparatively weaker, even though a slight positive correlation is seen.

Turbine loads are seen to generally increase with U_h. Compared with the maximum loads for OoPBM and FATBM (not shown), TTYM loads are somewhat less sensitive to changes in U_h; there are only a few simulations with load values above the 80% level (black dots) of the entire load range that result when the longitudinal wind speed, U_h, is greater than 12 m/s. This is because TTYM has a greater influence from the localized vertical wind velocity mean and turbulence (Figure 11) near the turbine hub and is relatively less affected by U_h. This finding is consistent with conclusions drawn from the regression model where, for TTYM MAX (relative to OoPBM MAX and FATBM MAX), the lowest coefficient for U_h was estimated and also this coefficient relative to coefficients for σ_W and W_h was diminished.

The relationship between turbine loads and wind velocity fields accompanying ABLs of different stability has also been studied by Churchfield et al[29] by performing two-point correlations between measured time series of turbine loads and streamwise wind velocity at selected probes. The results revealed that OoPBM loads are well-correlated with the streamwise wind velocity whereas TTYM loads are not. Conclusions were drawn that lift forces, roughly proportional to the incoming streamwise wind velocity, predominantly influence flapwise bending moments and result in the noted correlation. Yaw moments, associated with asymmetric loading on the rotor, cannot be assessed by a one-point measurement. In the present study, we assess relations between inflow and loads using simulation data from multiple LES runs followed by FAST aeroelastic analyses. Our results are consistent with those from the observational measurements. We found that longitudinal parameters (ie, U_h and σ_U) influence

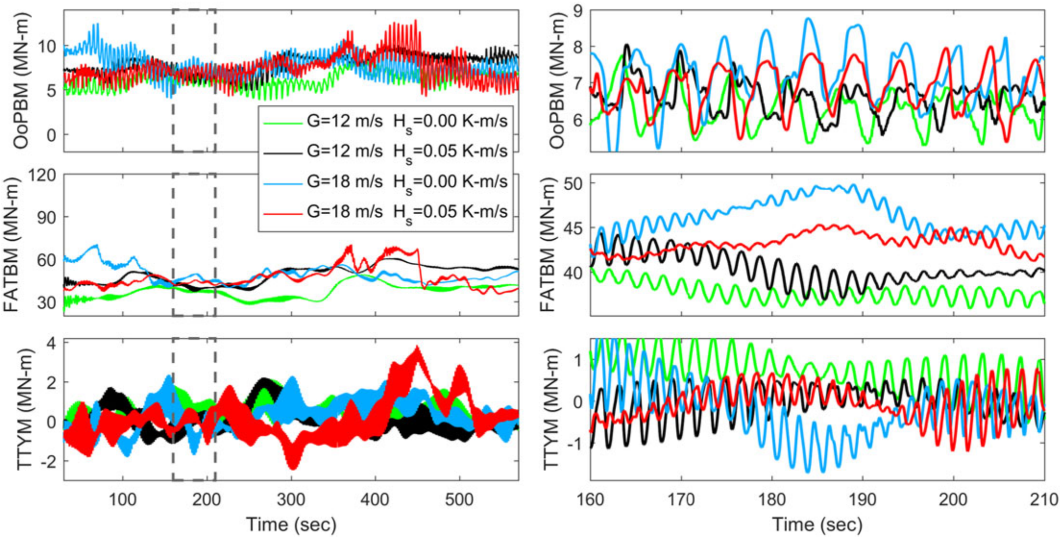

FIGURE 13 Comparison of time series of turbine loads for cases with different geostrophic wind speeds and surface heat fluxes [Colour figure can be viewed at wileyonlinelibrary.com]

OoPBM loads. The vertical wind components (W_h and σ_W) and the wind shear (α) tend to bring about asymmetric loading and, thus, contribute more to TTYM loads. The hub height longitudinal wind speed, U_h, is still seen to have a significant influence on TTYM loads as it provides the main force contribution that increases loading when the rotor is deformed in any asymmetric mode. Investigating the time-varying flow angle to the turbine blades, Nandi et al[30] concluded that horizontal fluctuations in the atmospheric winds influence OoPBM loads; this is consistent with our own finding that σ_U has significant influence on OoPBM fatigue loads.

4.3 | Influence of external variables on turbine loads

Next, we discuss how the full-domain "external" field variables (ie, the geostrophic wind speed and surface heat flux) influence the aeroelastic response of the turbine. We compare time series of the three load types first for different cases (G = 12 and 18 m/s; H_s = 0.00 and 0.05 K-m/s) in Figure 13. Time-domain simulation data from a selected 10-minute duration are shown in the left panels while the right panels show time series for an extracted shorter 50-second segment. In general, no clear trends in load levels are obvious since the time series fluctuate greatly. The influence of pitch control action in the G = 18 m/s cases also obscures relationships between simulated load levels and the external variables. Nevertheless, in the extracted 50-second segment of OoPBM time series, increasing geostrophic wind speed is seen to cause larger amplitudes of oscillations (with a period of about 5 seconds, which matches the 1P frequency of about 0.2 Hz). Similarly, in the TTYM time series, the cyclic amplitudes generally get larger as the geostrophic wind speed increases. The frequency of these oscillations is about 3P because of

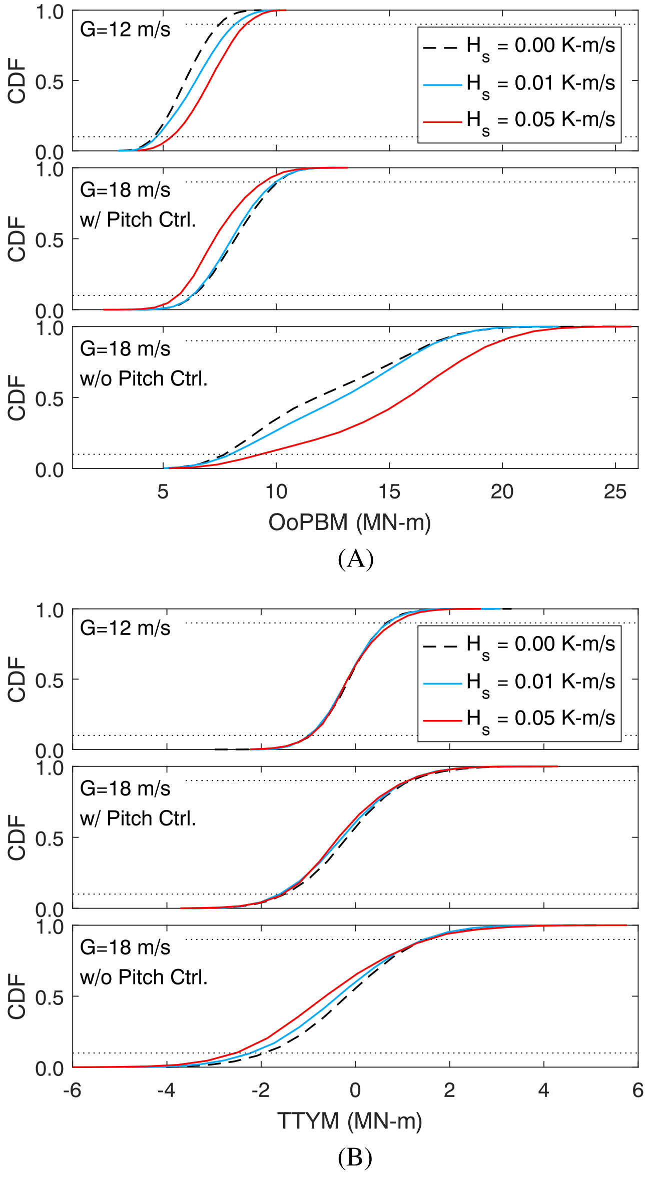

(A)

(B)

FIGURE 14 Cumulative distribution functions for A, OoPBM and B, TTYM loads for the cases with G = 12 and 18 m/s. The 1-hour time series of five extracted turbine-scale flow fields are used for the three cases with the different surface heat fluxes. Dotted lines are drawn at 0.10 and 0.90 quantiles [Colour figure can be viewed at wileyonlinelibrary.com] the asymmetric loading from the three blades which affects the nacelle yaw.[31] In the case of the FATBM, oscillations occur at a period of about 3 seconds, which corresponds to the fundamental period of the tower fore-aft bending mode of vibration. The amplitudes are almost the same for all four cases. The effect of changes in surface heat flux are not very clear from studying the load time series; they are further studied by statistical analyses and by examining power spectra of the load processes.

Figure 14 compares CDFs using data from 1-hour time series of OoPBM and TTYM loads for combinations of various G (12 and 18 m/s) and H_s (0.00, 0.01, and 0.05 K-m/s) values. The cases of $G = 18$ m/s without pitch control are also included in the bottom panels for the two loads. (For the sake of brevity and to highlight contrasts among the three load types, the FATBM CDFs are not included.) The CDFs shown are based on loads data obtained from all the five extracted turbine-scale inflow fields of each LES run. We notice first that increasing geostrophic wind speed tends to move the CDFs toward higher OoPBM load levels but has relatively little effect on moving the CDFs of the TTYM loads. Also, as the geostrophic wind speed is increased, CDFs for both OoPBM and TTYM loads cover a wider range, implying larger maximum loads (longer tails of the CDFs). One can assess this range by examining the load differences at CDF values equal to 0.10 and 0.90 (the horizontal dotted lines). It is clear that the $G = 18$ m/s cases have larger load differences than the $G = 12$ m/s cases. In contrast with the direct influence of geostrophic wind, an increase in surface heat flux results in almost no change to the CDFs for TTYM although it moves the CDFs for OoPBM very slightly—toward higher load levels—as seen in the $G = 12$ m/s cases. This same trend is not evident in the $G = 18$ m/s case because the triggered pitch control actions limit such changes. The OoPBM CDFs are seen to move towards higher load levels with an increase in H_s, if the pitch control is inactive in the $G = 18$ m/s case (consistent with the $G = 18$ m/s case when pitch control is not an issue for below-rated hub height winds). Load variances are greatly enhanced when the turbine is not pitch-controlled; this results in wider and flatter CDFs that, in turn, lead to high maximum loads for both OoPBM and TTYM. The effect of the external variables on FATBM CDFs (again, not shown for the sake of brevity) is similar to that seen for OoPBM loads.

The influence of external variables on fatigue loads is also of interest in this study. Comparing load range histograms based on rainflow cycle-counting permits greater understanding of equivalent fatigue loads (EFL). Figure 15 compares OoPBM rainflow amplitude histograms for four cases involving the different combinations of geostrophic wind speed ($G = 12$ and 18 m/s) and surface heat flux ($H_s = 0.00$ and 0.05 K-m/s). The 1-hour load time series resulting from a selected turbine-scale flow field is used in each case. It is evident that high-amplitude cycles (ie, greater than 3 MN-m) are larger in number for the higher G cases. This greater number of high-amplitude cycles leads to larger mean values (red dashed lines) of load amplitudes; this, in turn, leads to larger EFL values as estimated using Equation (3). Surface heat flux changes do not have much of an effect on the load histograms; however, the number of high-amplitude cycles is somewhat larger as H_s is increased for both the $G = 12$ and 18 m/s cases. In summary, the surface heat flux is seen to have relatively minor influence on turbine fatigue loads. Rainflow cycle histograms for FATBM and TTYM (not shown for brevity) exhibit similar general characteristics as those for OoPBM.

We investigate next the influence of the external variables on turbine loads by studying the variation of the load statistics with time during the ET period. Figures 16 and 17 show the variation with time of turbine load statistics every 10 minutes during the simulated 1 hour of the evening

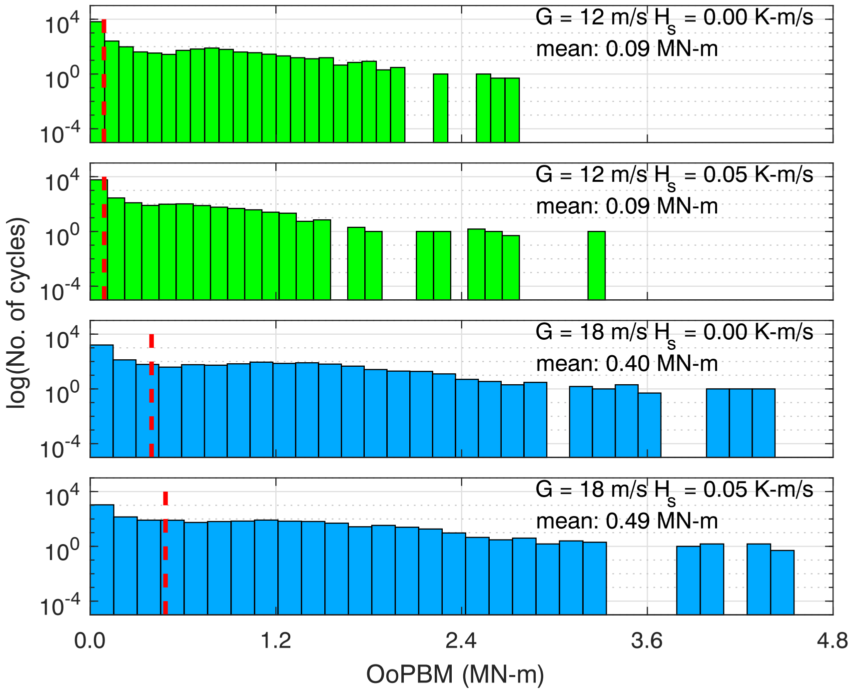

FIGURE 15 Rainflow cycle histograms of OoPBM loads for four cases involving different combinations of G and H_s. The data from selected turbine-scale slices from simulated 1-hour time series are used. Red dashed vertical lines denote mean values of the rainflow cycle-counted amplitudes [Colour figure can be viewed at wileyonlinelibrary.com]

transition for fatigue loads (left) and maximum loads (right) for selected LES cases. Error bars denote the standard deviations of the 10-minute data from the five extracted slices.

In Figure 16, we consider four different geostrophic wind speeds while holding the heat flux fixed at 0.00 K-m/s. In Figure 17, the geostrophic wind speed is held fixed at 12 m/s while the heat flux is changed. The black dashed line denotes the control case. In general, most of the loads are seen to decrease with time over 1 hour of the evening transition period. This can be attributed to the fact that the longitudinal mean wind speed at hub height (U_h) also decays with time over the one-hour simulation as seen in Figure 5. Since U_h has the most dominant influence on turbine loads, changes in other turbine-scale inflow variables (eg, an increased wind shear with time) do not greatly affect the decaying trend of loads during the evening transition. As seen in Figure 16, the decay in loads with time is the least for the G = 15 and 18 m/s cases which are influenced by pitch control actions. A limited range for the maximum level of the loads is clearly seen during the ET period evolution; the lines for the G = 15 and 18 m/s cases are close to each other, especially for the maximum OoPBM and FATBM loads.

It is evident from Figure 16 that larger loads result from increased geostrophic wind speeds. This is also consistent with conclusions drawn from Figures 14 and 15. Considering both fatigue and maxima, OoPBM loads appear to be most strongly correlated with geostrophic wind speed whereas TTYM loads indicate greater variability and obscure the trend. This is because the mean TTYM loads do not increase with increased G as was noted in Figure 14. The maximum loads increase due to an increase in variance of TTYM loads which cause greater fluctuations in load statistics. The FATBM EFL also shows great variability because its relation to U_h is the weakest among all the load statistics (as was noted in Figure 11); this, too, weakens the influence of G on FATBM EFL.

The influence of surface heat flux on turbine load statistics (as seen in Figure 17) is relatively weak compared with that of geostrophic wind speed. In the case of maximum loads, greater heat flux levels tend to cause higher values for OoPBM and FATBM. However, in the case of TTYM, this trend is not as clear. Furthermore, this trend is also not evident with the fatigue loads. An explanation for this requires consideration of wind shear. In Figure 11, we saw that wind shear contributes more to all three of the fatigue loads studied and to the TTYM maxima. We also saw that increased heat flux levels suppress or reduce wind shear (as discussed in Section 3.3); the competing effects of heat flux and shear lead to a weak

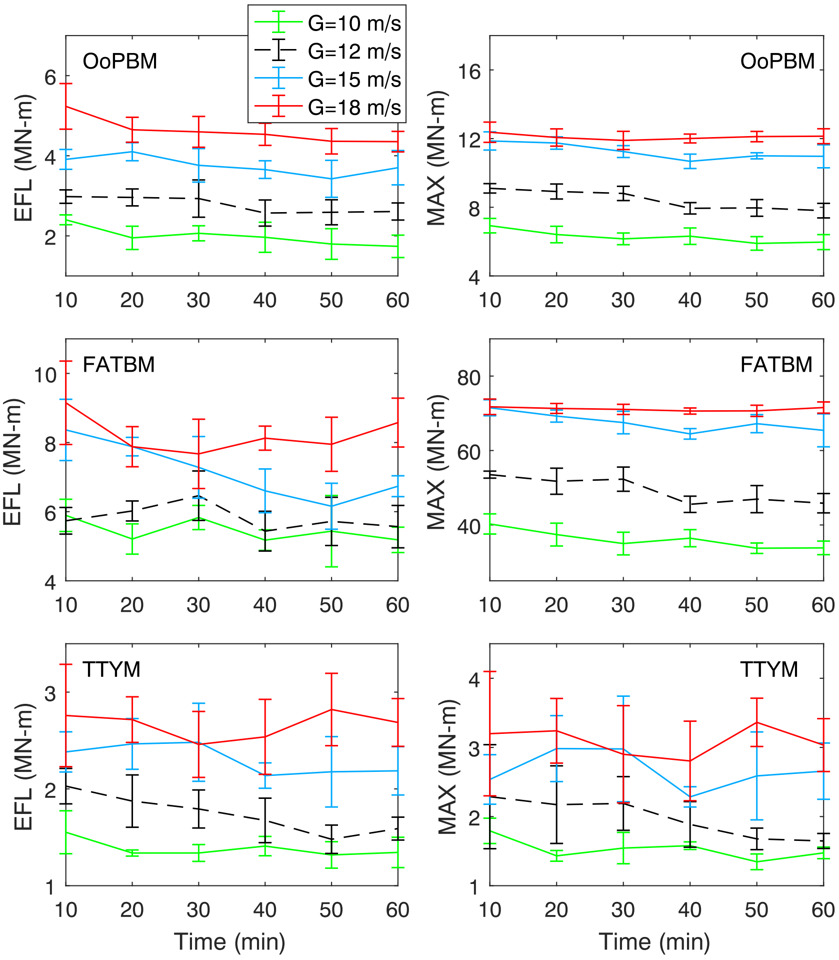

FIGURE 16 Variation of turbine load statistics with time for different geostrophic wind speeds (H_s = 0.00 K-m/s). Five 10-minute simulation samples from the five different lateral slices in the computational domain are used for each error bar (one standard deviation) [Colour figure can be viewed at wileyonlinelibrary.com]

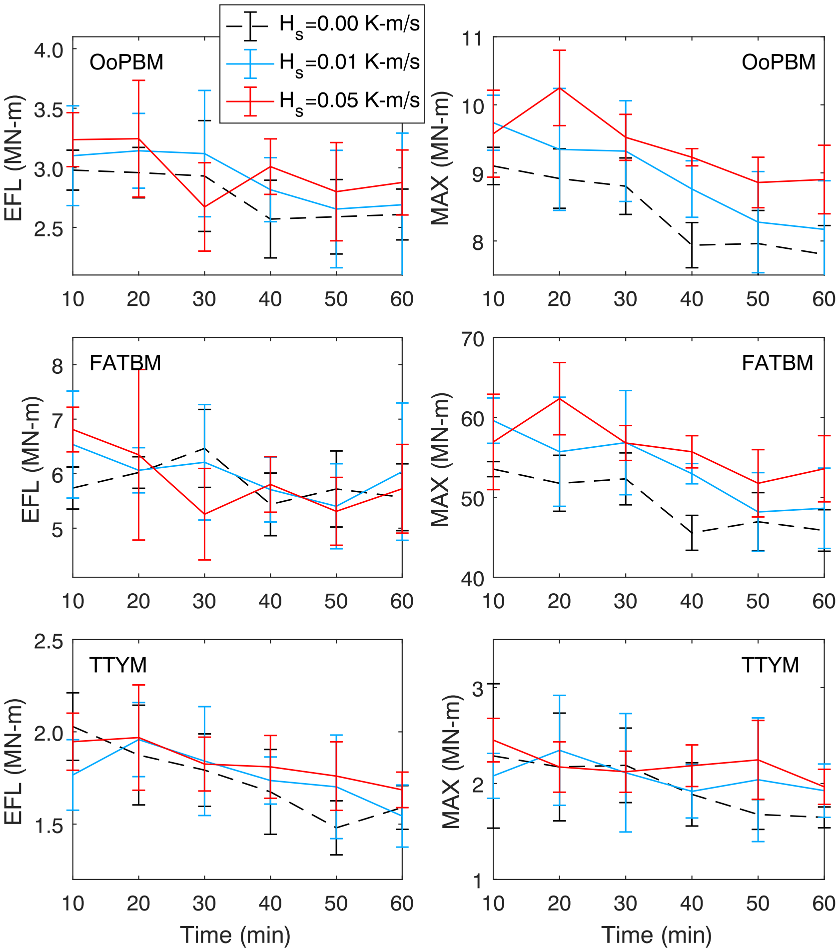

FIGURE 17 Variation of turbine load statistics with time for different heat fluxes (G = 12 m/s). Five 10-minute simulation samples from the five different lateral slices in the computational domain are used for each error bar (one standard deviation) [Colour figure can be viewed at wileyonlinelibrary.com]

influence of flux levels on turbine load statistics. This same conclusion may also be drawn from Figure 14 for the maximum load of TTYM and from Figure 15 for fatigue loads.

Churchfield et al[29] also compared OoPBM and TTYM loads in the ABL under neutral and unstable conditions; this work did not include a continuous transition. It was found that RMS levels of OoPBM are higher in the unstable case whereas, for TTYM, loads were either the same or reduced in the unstable case. Results from the present study are consistent with these findings, as seen in Figure 17. For the case with H_s = 0.00 K-m/s, which implies a neutral condition over the entire 1-hour period, the maximum OoPBM load is seen to be the lowest compared with the other two cases, which involve a transition from convective to neutral. Fatigue loads are also seen to be slightly lower for the neutral case with a less pronounced trend. The effect of stability is not very clear in TTYM load statistics, which is also consistent with the findings of Churchfield et al.[29] Because we rely on a continuously evolving period and present the statistical results using multiple flow fields and load data, the trends seen for turbine loads ABL flows of contrasting stability can be assessed systematically.

Figure 18 compares power spectra calculated from the entire 1-hour time series of longitudinal wind speed at hub height and the different turbine loads. The averaged spectrum of the five slices in the lateral direction is used. Data for four cases with combinations of different geostrophic wind speeds (G = 12 and 18 m/s) and surface heat fluxes (H_s = 0.00 and 0.05 K-m/s) are used. It is clearly seen in the wind speed spectra that there are energy drops at around 0.06 Hz for the G = 12 m/s cases and around 0.09 Hz for the G = 18 m/s cases. This is due to the limitation of grid resolution in the LES model and is deficient in energy in the high-frequency energy range as a result.[14] An increase in geostrophic wind speed from 12 to 18 m/s leads to increased energy over the 0.03 to 0.1 Hz frequency range. The results are consistent with the CDFs moving towards higher hub height wind speeds as the geostrophic wind speed increases, as seen in Figure 6. The effect of a change in surface heat flux on power spectra of U_h is relatively small. Energy in turbulence is seen to increase very slightly over a range of frequencies as the surface heat flux increases. Power spectra for TTYM show similar but less pronounced energy drops at frequencies corresponding to the drops in the wind speed spectra. An increase in geostrophic wind speed also causes greater energy in roughly the same frequency range as for U_h. Furthermore, it moves the spectral peak at the 3P frequency (~0.5 to 0.6 Hz, three times of the rotor rotational frequency 1P) toward higher frequencies. Yaw moments at the 3P frequency arise due to unbalanced aerodynamic forces applied on the three blades; this frequency can increase with larger wind velocities. In the power spectra for OoPBM and FATBM, differences in energy resulting from changes in geostrophic

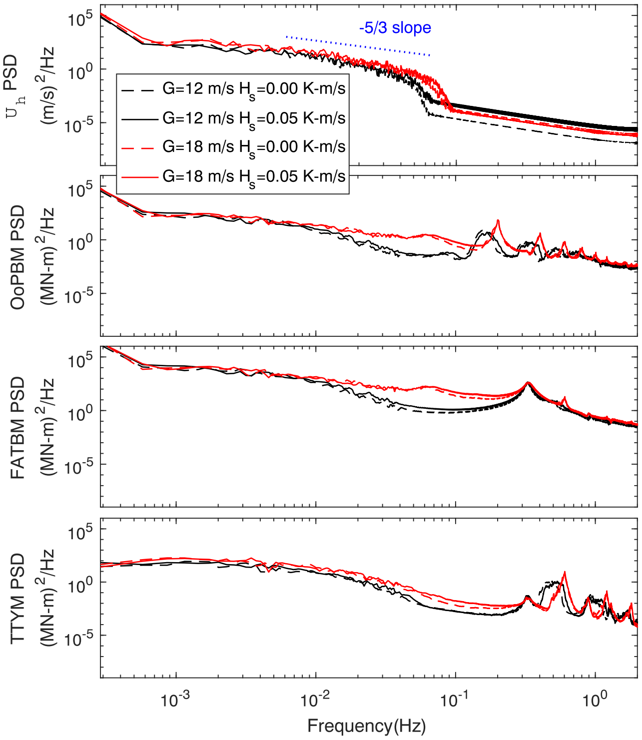

FIGURE 18 Comparison of power spectra of hub height longitudinal wind speeds and turbine loads for selected 1-hour time series using an average of the five slices in the lateral direction. Four cases with combinations of various *G* and H_s are considered [Colour figure can be viewed at wileyonlinelibrary.com]

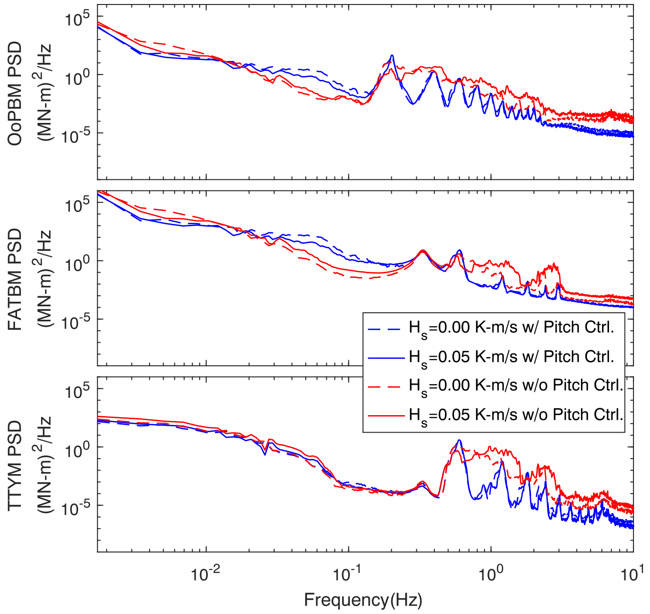

FIGURE 19 Comparison of power spectra of turbine loads for the selected cases of $G = 18$ m/s with $H_s = 0.00$ K-m/s (dashed curves) and 0.05 K-m/s (solid curves) using selected 1-hour time series with an average of the five slices in the lateral direction. The blue and red curves correspond to cases with and without pitch control, respectively [Colour figure can be viewed at wileyonlinelibrary.com]

wind speed are mainly seen over an intermediate frequency range (ie, ~0.01-0.1 Hz for OoPBM and ~0.01-0.3 Hz for FATBM). The harmonics of the rotor rotational frequency (1P, 2P, 3P, etc) are clearly seen in the OoPBM power spectra. The frequencies associated with these spectral peaks move toward higher values as the geostrophic wind speed increases. The fundamental frequency for tower fore-aft bending, which is in the range 0.3 to 0.4 Hz, is evident in both the FATBM and TTYM power spectra. The peak is consistent with the natural frequency of the first tower fore-aft bending mode for the 5-MW turbine for the onshore configuration (ie, 0.3240 Hz). In the FATBM spectra, there is also a small 3P spectral peak which moves to higher frequencies with increase in *G*. Findings based on studies of the load time series (Figure 13) are consistent with the power spectra in that the amplitudes of the peaks in the OoPBM and TTYM spectra occur at slightly higher frequencies as *G* is increased;

on the other hand, the fundamental fore-aft bending mode frequency in the FATBM power spectra is the location of a spectral peak that does not change as G is increased. Again, the effect of changes in surface heat flux is not evident in the load power spectra; of course, any trend that might result from such changes may be obscured by the active pitch control in the G = 18 m/s cases.

To assess the influence of pitch control actions on the load power spectra, we compare spectra of all the loads for the cases of G = 18 m/s with and without pitch control in Figure 19. Frequencies associated with all the spectral peaks that arise from rotational sampling are seen to increase when pitch control is inactive; this occurs because pitch control enforces a constant rotor rotation rate of 12.1 rpm and keeps the 1P frequency at about 0.2 Hz. The energy in the low- and high-frequency range is greater in the absence of pitch control. In the power spectra when pitch control is inactive (red), it is found that greater surface heat flux can slightly increase energy over the 0.03 to 0.1 Hz frequency range for all loads. This same trend is not evident when pitch control is active (blue). An increase in surface heat flux also moves the 1P frequency peak in the OoPBM power spectra and the 3P frequency peaks in the FATBM and TTYM power spectra towards higher frequencies when pitch control is not active.

5 | CONCLUSIONS

In this study, we have described the development of an extensive database of high-resolution (~28 m), four-dimensional flow fields that represent the important evening transition (ET) period using an idealized LES model. This period is when energy demand peaks occur; it is also the period that often precedes thunderstorm activity. Full-domain atmospheric conditions (geostrophic wind speed) and surface boundary conditions (surface heat flux) were systematically varied to establish the database for subsequent statistical and spectral analyses. Turbine-scale wind field statistics (such as the hub height longitudinal wind speed, hub height turbulence standard deviation, and wind shear) were studied and their mutual correlations as influenced by variations in the external full-domain variables were discussed. In addition, we carried out statistical studies of different loads on a 5-MW wind turbine by using the LES-generated flow fields to create the inflow wind velocity fields for aeroelastic response simulations. A database of both fatigue and maximum load statistics was developed from the output load time series for the selected turbine model. A multivariate regression model was developed to assess contributions from the different turbine-scale wind field variables to the load statistics; these in turn were used to assess the effects of external variables and the interplay with the blade pitch control system. It is concluded that the geostrophic wind speed and heat flux both influence turbine loads to different degrees. We acknowledge that the ~28 m spatial resolution is at the limit for achieving acceptably accurate loads for the 5-MW turbine but the important structural modes of vibration are accounted for. For this study, which examines different atmospheric stability conditions during the ET period, the spatial resolution may be adequate in some but not all cases of the different degrees of implied mixing and turbulence; in some cases, a finer resolution might be warranted but for the sake of comparison and for ease in handling similar-sized output, no customized adjustments were made for convergence in the 12 cases. We also note that there are significant computational challenges associated with the use of LES for a large computational domain with a spatial resolution finer than ~28 m resolution, especially when using a pseudo-spectral code with a dynamic SGS model. The essential knowledge gained from this study about the wind field during the ET period is summarized here from two angles—the geostrophic wind and the heat flux.

First, increases in the geostrophic wind speed enhance the full-domain wind field around the turbine which, in turn, increases the mean and variance of the longitudinal wind speeds at hub height (ie, U_h and σ_U) as well as the turbine-scale wind shear (α). As the geostrophic wind speed increases, the mean and variance of turbine loads also increase (with the exception of TTYM mean) and result in higher maximum loads. All the fatigue loads also get larger with an increase in geostrophic wind speed since this increase causes more high-amplitude stress cycles as found following rainflow-cycle counting on the loads time series. Larger geostrophic wind speeds also lead to higher spectral peaks and higher frequencies associated with the peaks arising from rotational sampling; the larger amplitudes of periodic fluctuations in time series of OoPBM and TTYM loads are consistent with this finding. Blade pitch control activated in the larger geostrophic wind speed cases results in the suppression of load maxima. In sum, an increased geostrophic wind speed basically elevates the mean wind level which in turn causes larger loads and greater risks of turbine fatigue damage; however, yaw moments are not greatly influenced by increased geostrophic winds since they do not cause large asymmetric loading even though the turbulence intensity is also increased.

Next, we consider the influence of surface heat flux. We find that increases in heat flux distort the full-domain wind field around the turbine and lead to larger U_h but smaller α values. The mixing brought about at the surface causes enhanced vertical turbulence but little change streamwise. Since all the fatigue loads as well as the TTYM maximum load are influenced by wind shear, the larger U_h and smaller α values result in competing effects when surface heat flux is increased. As a result, surface heat flux changes only have an effect on the maximum OoPBM and FATBM loads. Surface heat flux changes also have relatively little influence on load range histograms resulting from rainflow cycle counting or on the power spectra of all loads. In brief, an increasing surface heat flux can result in larger maxima for those turbine loads that are not sensitive to wind shear, since wind shear is found to be weaker in the (more convective) ABL.

Based on the results of this study, the LES-ABL simulation framework is seen to successfully capture characteristics of the evening transition from a convective to a neutral boundary layer. The wind field and turbine load statistics suggest that the longitudinal mean wind speed and vertical turbulence as well as associated turbine loads (in the absence of pitch control) generally decay over the 1-hour period representing the evening transition. These investigations on the wind fields during the evening transition are considered to be fundamental to our understanding of precursor downburst scenarios that often occur in the late-afternoon and early-evening hours.[32]

The change in atmospheric stability is one of the distinctive characteristics of ET fields that influences atmospheric mixing and turbulence intensity in the ABL. The extent of turbulence in the wind fields can affect the strength of air cushions when downbursts touch down and form impinging jets near the ground. The interaction with ambient turbulence also affects the strength and development rate of associated outburst winds.[33] The relationships between stability change and turbine-scale flow field variables (ie, Section 3.2) is expected to be of interest when the impact of downburst winds on turbine loads is to be estimated. Sudden changes in these turbine-scale variables due to downburst strikes can be further investigated and compared with their values during the ET period. Since we have studied how characteristics of ET wind fields affect turbine loads as well as the interplay with blade pitch control (Section 4), similar loads studies under nonstationary downburst winds can be more clearly contrasted with loads during the ET period. The effect and benefits of pitch control during downbursts can also be compared with that in the ET period. Following from this study, we expect to refine the evaluation of downburst wind field characteristics and associated turbine loads after incorporating appropriate but variable conditions during the precursor evening transition; in this way, we can further improve the design for wind turbines under such peak loading scenarios.

ACKNOWLEDGEMENTS

The authors gratefully acknowledge the financial support received from the National Science Foundation (NSF) under Grant Nos. CBET-1336304 and CBET-1336760.

ORCID

Sukanta Basu https://orcid.org/0000-0002-0507-5349
Lance Manuel https://orcid.org/0000-0002-0602-3014

REFERENCES

1. Wind turbine generator system - part 1: Design requirements, 3rd edn. IEC 61400-1, Geneva, Switzerland, International Electrotechnical Commission; 2005.
2. Mahrt L. The early evening boundary layer transition. *Q J R Meteorol Soc.* 1981;107(452):329-343.
3. Grant ALM. An observational study of the evening transition boundary-layer. *Q J R Meteorol Soc.* 1997;123(539):657-677.
4. Ruiz-Columbie A. Atmospheric boundary layer evening transitions over West Texas. *Ph.D. Thesis*: Texas Tech University; 2008.
5. Sastre M, Yagüe C, Román-Cascón C, Maqueda G. Atmospheric boundary-layer evening transitions: a comparison between two different experimental sites. *Bound-Lay Meteorol.* 2015;157(3):375-399.
6. CAISO. What the duck curve tells us about managing a green grid, California Independent System Operator, Report No. CommPR/2016, Folsom, CA, 2016.
7. Nieuwstadt FTM, Brost RA. The decay of convective turbulence. *J Atmos Sci.* 1986;43(6):532-546.
8. Sorbjan Z. Decay of convective turbulence revisited. *Bound-Lay Meteorol.* 1997;82(3):503-517.
9. Pino D, Jonker HJJ, De Arellano JV-G, Dosio A. Role of shear and the inversion strength during sunset turbulence over land: characteristic length scales. *Bound-Lay Meteorol.* 2006;121(3):537-556.
10. Rizza U, Miglietta MM, Degrazia GA, Acevedo OC, Marques Filho EP. Sunset decay of the convective turbulence with large-eddy simulation under realistic conditions. *Physica A*. 2013;392(19):4481-4490.
11. Rizza U, Miglietta MM, Acevedo OC, et al. Large-eddy simulation of the planetary boundary layer under baroclinic conditions during daytime and sunset turbulence. *Meteorol Appl.* 2013;20(1):56-71.
12. Jayaraman B, Brasseur J. Transition in atmospheric turbulence structure from neutral to convective stability states. In: 32nd ASME Wind Energy Symposium: National Harbor, MD. 2014. https://doi.org/10.2514/6.2014-0868
13. Jonkman B. TurbSim user's guide: Version 1.50. Technical Report NREL/TP-500-46198, Golden, CO, National Renewable Energy Laboratory; 2009.
14. Sim C, Basu S, Manuel L. On space-time resolution of inflow representations for wind turbine loads analysis. *Energies*. 2012;5(7):2071-2092.
15. Park J, Manuel L, Basu S. Toward isolation of salient features in stable boundary layer wind fields that influence loads on wind turbines. *Energies*. 2015;8(4):2977-3012.
16. Park J, Basu S, Manuel L. Large-eddy simulation of stable boundary layer turbulence and estimation of associated wind turbine loads. *Wind Energy*. 2014;17:359-384.
17. Geurts BJ. *Elements of direct and large-eddy simulation*. Philadelphia: Edwards; 2003.
18. Basu S, Porté-Agel F. Large-eddy simulation of stably stratified atmospheric boundary layer turbulence: a scale-dependent dynamic modeling approach. *J Atmos Sci.* 2006;63(8):2074-2091.
19. Basu S, Vinuesa JF, Swift A. Dynamic LES modeling of a diurnal cycle. *J Appl Meteorol Climatol.* 2008;47(4):1156-1174.
20. Jonkman J, Butterfield S, Musial W, Scott G. Definition of a 5-MW reference wind turbine for offshore system development, Golden, CO., National Renewable Energy Laboratory (NREL); Technical Report NREL/TP-500-38060, 2009.
21. Jonkman J, Buhl Jr ML. FAST user's guide. Technical Report NREL/EL-500-38230, Golden, CO, National Renewable Energy Laboratory; 2005.
22. Jonkman B, Jonkman J. Readme file for FAST v8. 08.00 c-bjj. National Renewable Energy Laboratory; 2014.
23. Bir G, Jonkman J. Aeroelastic instabilities of large offshore and onshore wind turbines. In: Journal of physics: Conference series, Vol. 75 IOP Publishing; 2007; Technical University of Denmark, Kongens Lyngby, Denmark: 12069.

24. Rai RK, Gopalan H, Naughton JW. Effects of spatial and temporal resolution of the turbulent inflow on wind turbine performance estimation. *Wind Energy*. 2016;19(7):1341-1354.
25. Glendening JW, Haack T. Influence of advection differencing error upon large-eddy simulation accuracy. *Bound-Lay Meteorol*. 2001;98(1):127-153.
26. Sutherland HJ. On the fatigue analysis of wind turbines. Technical Report SAND99-0089, Albuquerque, New Mexico, Sandia National Laboratories; 1999.
27. Nguyen HH, Manuel L, Jonkman J, Veers PS. Simulation of thunderstorm downbursts and associated wind turbine loads. *J Sol Energy Eng*. 2013;135(2):21014.
28. Nguyen HH, Manuel L. Transient thunderstorm downbursts and their effects on wind turbines. *Energies*. 2014;7(10):6527-6548. http://www.mdpi.com/1996-1073/7/10/6527
29. Churchfield MJ, Lee S, Michalakes J, Moriarty PJ. A numerical study of the effects of atmospheric and wake turbulence on wind turbine dynamics. *J Turbul*. 2012;2012(13):N14.
30. Nandi TN, Herrig A, Brasseur JG. Non-steady wind turbine response to daytime atmospheric turbulence. *Phil Trans R Soc A*. 2017;375:20160103.
31. Lee S, Churchfield MJ, Moriarty PJ, Jonkman J, Michalakes J. A numerical study of atmospheric and wake turbulence impacts on wind turbine fatigue loadings. *J Sol Energy Eng*. 2013;135(3):31001.
32. Wakimoto RM. Convectively driven high wind events. *Severe convective storms*. Boston, MA: Springer, American Meteorological Society; 2001:255-298.
33. Hawbecker P, Basu S, Manuel L. Investigating the impact of atmospheric stability on thunderstorm outflow winds and turbulence. *Wind Energy Sci*. 2018;3(1):203.
34. Chow FK, Street RL, Xue M, Ferziger JH. Explicit filtering and reconstruction turbulence modeling for large-eddy simulation of neutral boundary layer flow. *J Atmos Sci*. 2005;62(7):2058-2077.
35. Anderson WC, Basu S, Letchford CW. Comparison of dynamic subgrid-scale models for simulations of neutrally buoyant shear-driven atmospheric boundary layer flows. *Environ Fluid Mech*. 2007;7(3):195-215.

How to cite this article: Lu N-Y, Basu S, Manuel L. On wind turbine loads during the evening transition period. *Wind Energy*. 2019;22:1288–1309. https://doi.org/10.1002/we.2355

APPENDIX A: VARIATION OF STABILITY STATE

In Figure A1, we show the variation of the dimensionless stability parameter, $-z_i/L$, with time through the second hour in the simulations, where z_i represents the boundary layer height defined by the height of the minimum planar-averaged sensible heat flux, and L represents the Obukhov length defined by

$$L = -\frac{\theta_0 u_*^3}{\kappa g q_s}, \tag{A1}$$

where θ_0 is the reference potential temperature equal to 300 K; κ is the von Kármán constant set to 0.4; q_s is the prescribed surface heat flux that varies from H_s to zero during the second hour of the simulations. Also, u_* is the friction velocity defined by

$$u_* = \left(\langle u'w'\rangle_s^2 + \langle v'w'\rangle_s^2\right)^{0.25}, \tag{A2}$$

where $\langle u'w'\rangle_s$ and $\langle v'w'\rangle_s$ represent the planar-averaged momentum flux components at the surface layer. Four nonneutral cases with combinations of different G and H_s values are presented for comparison. The results reveal that instability decreases with time during the evening transition in all cases; $-z_i/L$ decreases to zero with time since the surface heat flux also decreases to zero. In addition, the figure also shows that a higher surface sensible heat flux causes greater instability while a higher geostrophic wind causes less instability. The boundary layer height, z_i, is also presented in Figure A1 and suggests an increasing trend with time resulting from continuous addition of heat flux at the surface. Higher values of both H_s and G lead to deeper z_i values, as would be physically expected.

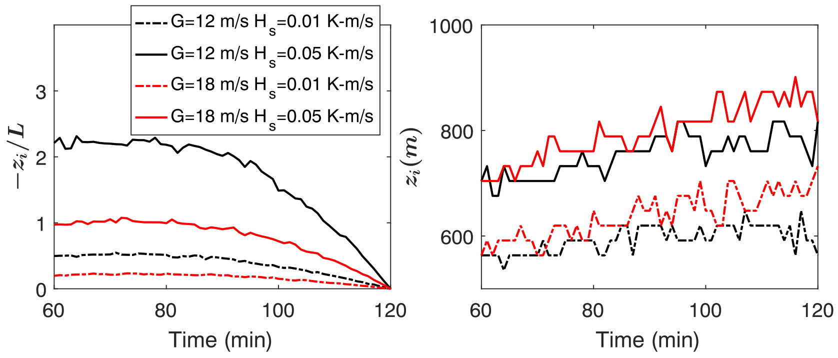

FIGURE A1 Comparison of the variation of stability state (left panel) and boundary layer height (right panel) during the second hour of simulation time. Four cases with different combinations of G and H_s values are considered [Colour figure can be viewed at wileyonlinelibrary.com]

APPENDIX B: NEAR-WALL CHARACTERISTICS FOR THE NEUTRAL CASE

Figure B1 compares vertical velocity profiles with a log-law profile for all the neutral cases in order to examine the law-of-the-wall scaling. For horizontal-averaged and time-averaged "total" wind speed, $\langle \overline{U_T} \rangle$ (ie, $U_T = \sqrt{U^2 + V^2}$), the log law is written as follows:

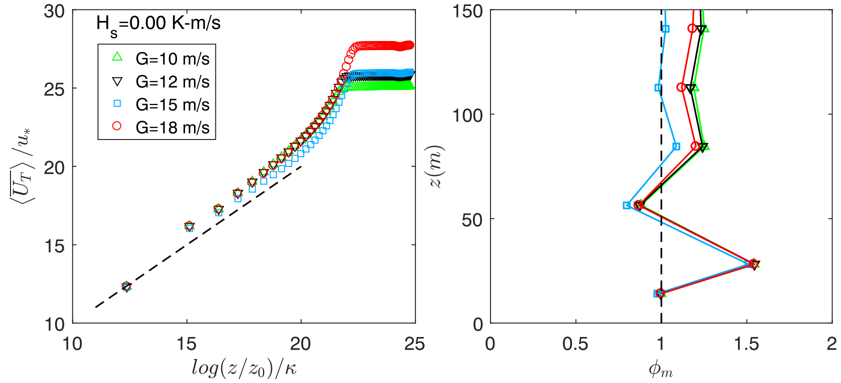

FIGURE B1 Comparison of horizontal- and time-averaged velocity profiles (left panel) and dimensionless velocity gradient, $\phi_m(z)$ (right panel) for the cases of H_s = 0.00 K-m/s, with different geostrophic wind speeds [Colour figure can be viewed at wileyonlinelibrary.com]

$$\frac{\langle \overline{U_T} \rangle}{u_*} = \frac{1}{\kappa} \log \frac{z}{z_0}. \tag{B1}$$

Since the initial boundary layer height, H_i, is set to 500 m (and it grows marginally under neutral condition), the surface layer is expected no higher than ~50 m (ie, 10% of H_i). Thus, no more than 2 to 3 grid points are expected to lie within the surface layer based on the grid resolution of ~28 m. The results show reasonable near-wall characteristics in the LES model employed. The dimensionless velocity gradient

$$\phi_m = \kappa \frac{z}{u_*} \frac{\partial \langle \overline{U_T} \rangle}{\partial z}, \tag{B2}$$

which should be equal to unity in the surface layer of NBL, is also presented in Figure B1.

In the literature, LES runs for NBLs are usually conducted for long periods of time (~30 h) so that the statistics converge properly. Since we are interested in the evening transitional period, we could not extend our runs beyond a 2-hour period. In spite of this unavoidable limitation, our results (including the "overshoot" behavior) are quite comparable with those in the existing literature.[34,35] We wish to emphasize that even with a relatively coarse resolution of ~28 m, the dynamic SGS model (LASDD) was able to capture the expected log-law behavior.

APPENDIX C: LARGE-SCALE COHERENT STRUCTURE

Figure C1 shows coherent structures of the velocity fields in the longitudinal and vertical directions for the control case (G = 12 m/s, H_s = 0.00 K-m/s). Cross-sections at a height, z =~100 m, are selected for both wind velocity components. In the U-wind field, a streaky structure is evident parallel to the mean wind direction. More detailed discussions about such streaky structures can be found in Anderson et al.[35] For the vertical wind field, the flow pattern is rather incoherent.

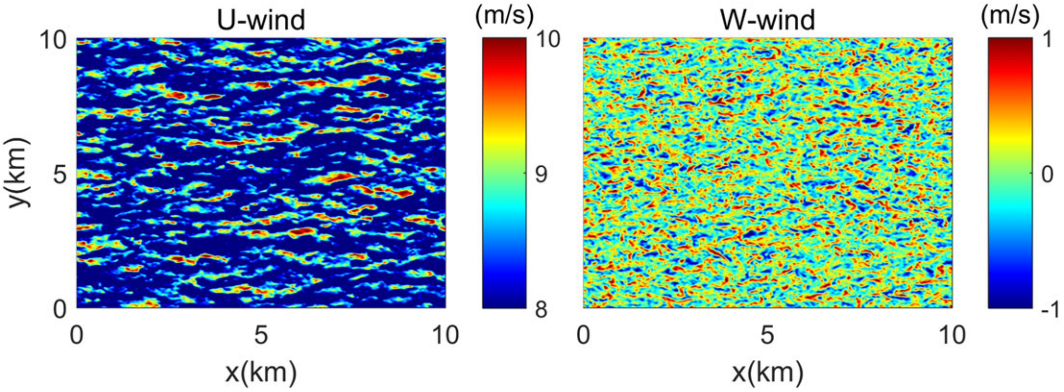

FIGURE C1 Visualization of velocity fields in the longitudinal (left panel) and vertical (right panel) directions for the control case (G = 12 m/s, H_s = 0.00 K-m/s), cross-sectioned at the height, z =~100 m [Colour figure can be viewed at wileyonlinelibrary.com]

In this study, we used a spatial resolution of ∼28 m where the effective temporal resolution is about 20 sec (∼1/0.05 Hz based on Figure 18). This resolution is not sufficient for the computation of coherence values at small scales.